JOURNAL OF COMPUTATIONAL PHYSICS **146,** 58–81 (1998)
ARTICLE NO. CP985955

A Flux-Split Algorithm Applied to Relativistic Flows

R. Donat,* J. A. Font,†,‡ J. Mª Ibáñez,‡ and A. Marquina*

**Departamento de Matemática Aplicada, Universidad de Valencia, 46100 Burjassot, Valencia, Spain;*
†Max-Planck-Institut für Gravitationsphysik, Schlaatzweg 1, D-14473 Potsdam, Germany;
and ‡Departamento de Astronomía y Astrofísica, Universidad de Valencia,
46100 Burjassot, Valencia, Spain

Received May 27, 1997; revised January 5, 1998

The equations of RFD can be written as a hyperbolic system of conservation laws by choosing an appropriate vector of unknowns. We give an explicit formulation of the full spectral decomposition of the Jacobian matrices associated with the fluxes in each spatial direction, which is the essential ingredient of the techniques we propose in this paper. These techniques are based on the recently derived flux formula of Marquina, a new way to compute the numerical flux at a cell interface which leads to a conservative, upwind numerical scheme. Using the spectral decompositions in a fundamental way, we construct high order versions of the basic first-order scheme described by R. Donat and A. Marquina in (*J. Comput. Phys*. **125**, 42 (1996)) and test their performance in several standard simulations in one dimension. Two-dimensional simulations include a wind tunnel with a flat faced step and a supersonic jet stream, both of them in strongly ultrarelativistic regimes.

Key Words: non-linear systems of conservation laws; shock capturing; special relativistic hydrodynamics.

1. INTRODUCTION

The term relativistic fluid dynamics applies to both those flows in which the velocities (of individual particles or of the fluid as a whole) approach c, the velocity of light in vacuum, or those where the effects of the background gravitational field—or that generated by the matter itself—are so important that a description in terms of Einstein theory of gravity becomes necessary.

In recent years, relativistic fluid dynamics (RFD henceforth) has come to play an important role in science. In nuclear physics, heavy-ion collision experiments taking place nowadays in large particle accelerators produce beams with velocities equal to a large fraction of c. Nuclear collisions are described in the language of relativistic hydrodynamics as a

0021-9991/98 $25.00

solution of an initial value problem. After the nuclei collide, compression shock waves form in the nuclear matter. The aim of these experiments is to gain insight into the equation of state of hot dense matter (see, e.g., the review in [29] or Strottman's talk in [30]). Currently, energies of more than 100 GeV/nucleon are obtained (i.e., Lorentz factors larger than 100) and the TeV regime is planned in future experiments.

Almost any high energy astrophysical phenomenon requires a relativistic treatment. Scenarios involving compact objects as supernovae, active galactic nuclei, and coalescing compact binaries include flows at relativistic speeds and the presence of strong shock waves. In particular, flow velocities as large as 99% of c are required to explain the apparent superluminal motion observed in many of the commonly observed jets in extragalactic radio sources associated to active galactic nuclei (two superluminal sources have been recently identified in our Galaxy [28]). The observational evidences in these systems confirm that Lorentz factors greater than 10 are plausible (see, e.g., [22] and references therein).

The evolution of a relativistic fluid is described by a system of equations which are the expression of *local conservation laws*: the local conservation of baryon number density, and the local conservation of energy-momentum

$$\nabla_\mu(\rho U^\mu) = 0, \quad \nabla_\mu T^{\mu\nu} = 0 \tag{1}$$

(throughout the paper, Greek indices run from 0 to 3, Latin indices from 1 to 3, and units in which the speed of light is equal to one are used). Here, ρ is the rest-mass density, U^μ the 4-velocity vector and ∇_μ stands for the covariant derivative. The energy-momentum tensor, $T^{\mu\nu}$, describes the physical properties of matter. For example, for a perfect fluid

$$T^{\mu\nu} = \rho h U^\mu U^\nu + p g^{\mu\nu}, \tag{2}$$

where p is the pressure and h is the specific enthalpy, defined as

$$h = 1 + \varepsilon + p/\rho, \tag{3}$$

with ε being the specific internal energy. The tensor $g^{\mu\nu}$ defines the metric of the space-time $\mathcal{M}$ where the fluid evolves.

The RFD equations are hyperbolic, just as their Newtonian counterparts, which is the mathematical manifestation of the fact that information takes time to spread in space-time. An immediate consequence of a finite speed of propagation is the possibility of discontinuities in the solution of the system of partial differential equations.

Simulations based on the numerical integration of the hydrodynamical equations provide a valuable tool to confront the theoretical models with the observations (as in astrophysics) or the experimental results (as in nuclear physics), which explains the rapid progress, during the last few years towards the development of reliable RFD-codes that work accurately under the extreme conditions of interest.

The first Eulerian code in RFD was developed by Wilson [32], on the basis of explicit finite-differencing techniques and monotonic transport. The code incorporated artificial viscosity techniques based on earlier work of Richtmyer and Morton [25] for the nonrelativistic flow equations. Wilson's code and its sequels have been widely used in cosmology, axisymmetric relativistic stellar collapse, accretion onto compact objects, collisions of heavy ions and, more recently, in studies of coalescing compact binaries. However, despite its popularity (almost all codes in numerical relativistic hydrodynamics in the eighties were based

in Wilson's procedure—see, e.g., Refs. in [3]) it turned out to be unable to resolve the extremely strong shock structures that appear in the ultrarelativistic regime.

Norman and Winkler analyzed in depth the artificial viscosity approach to RFD in [23]. Their research led them to the conclusion that a fully implicit treatment of the relativistic equations was the only way to increase the accuracy of artificial viscosity formulations in the ultrarelativistic regime.

By the mid-eighties and fueled by an increasing awareness that the artificial viscosity approach was of limited use in the ultrarelativistic regime, part of the numerical RFD community started to look into other shock capturing techniques that had been successfully applied in gas dynamics to obtain accurate numerical approximations in the presence of strong shocks.

Over the last few decades, many shock-capturing methods have arisen in classical gas dynamics simulations. Nowadays, state-of-the-art numerical simulations employ high resolution shock capturing (HRSC henceforth) methods. HRSC techniques produce highly accurate numerical approximations (formally second order or better) in smooth regions of the flow and capture the motion of unresolved steep gradients, without creating spurious oscillations. Typically, these techniques require a deeper knowledge of the physics of the system than the artificial viscosity approach, but the resulting numerical codes are more robust and less dependent on ad-hoc parameters.

Although most HRSC methods were developed with the Euler equations of gas dynamics in mind, they have now been carefully formulated within a systematic mathematical framework that makes them general purpose numerical methods for hyperbolic systems of conservation laws. This explains why the development of modern shock capturing codes in numerical RFD has followed the trail of Newtonian hydro-codes.

The first explicit shock capturing codes in RFD without artificial viscosity appear in the early nineties [17, 15, 8]. These codes follow the so-called "Godunov approach," and their design is based on two main points: (1) The ability to write the RFD equations as a system of hyperbolic conservation laws, identifying a suitable vector of unknowns. (2) An *approximate Riemann solver* built using the spectral decomposition of the Jacobian matrices of the system.

Nowadays, many of the most successful shock-capturing codes in gas dynamics have a relativistic extension. For example, and with no intent of being exhaustive, Eulderink [8] has explicitly derived a relativistic Roe Riemann solver, Schneider *et al.* [26] carried out the extension of Einfeldt's HLLE method, Martí and Müller [19] extended the PPM method of Woodward and Colella, Wen *et al.* [31] extended Glimm's method, Dolezal and Wong [6] have put into practice Shu-Osher ENO techniques, and Balsara [2] has extended Colella's two-shock approximation. With the help of these extensions, the realm of simulations of special-relativistic flows has begun to be explored within the last few years [5, 6, 9, 11, 12, 20–22, 19, 26].

From the results of many test calculations shown in the previous references, it is apparent that an accurate description of ultrarelativistic flows with strong shock waves can be accomplished by writing the RFD equations in conservation form and using the wealth of shock capturing techniques devised for Newtonian hydrodynamics.

HRSC methods are now routinely used in classical gas dynamics to discretize the convective derivatives of a general system of convection–diffusion–reaction equations in any number of spatial dimensions. It is well known, although not particularly well understood, that many of these shock-capturing techniques can, on occasions, fail quite spectacularly.

An excellent review on the numerical pathologies that can be encountered in gas dynamics simulations is given by Quirk [24]. Usually, the pathological behavior is local and does not cause the code to crash. However, in complicated situations, the pathological behavior that a particular scheme may display can have a disastrous effect on the numerical approximation: one example treating an interface separating a liquid drop—incompressible Navier–Stokes fluid—and a high speed gas—chemically reactive Navier–Stokes fluid—is described in [10].

As in Newtonian hydrodynamics, HRSC methods are starting to become part of numerical codes designed to model more complicated situations in RFD. In the references given above, many of the local pathologies observed in Newtonian hydrodynamics can also be observed in relativistic tests. It becomes, thus, important to be aware of the occurrence of any numerical pathologies in a given scheme.

In a recent paper [4], Donat and Marquina propose a numerical scheme for hyperbolic systems of conservation laws that produces numerical approximations less sensitive to the local pathologies mentioned in [24]. In the case described in [10], the use of Marquina's flux formula also results in a physically well-behaved numerical solution which appears free of (unwanted) oscillations.

In this paper, we provide the technical ingredients needed to implement Marquina's scheme for relativistic flows. In our numerical simulations in RFD, a sample of which shall be displayed in later sections, we observe that the behavior of the scheme is largely the same as in the classical gas dynamics case: Many of the (local) numerical pathologies encountered in some of the aforementioned references are considerably reduced or even eliminated.

The paper is organized as follows: In Section 2, we give an explicit ready-to-work description of the spectral decomposition of the multidimensional RFD system in conservation form. In Section 3 we describe briefly Marquina's technique. In order to demonstrate the capabilities of Marquina's scheme in the simulation of relativistic flows, in Section 4 we analyze a significant sample of the standard one-dimensional tests for which the exact solution is known. All tests in this section have also been carried out by other authors, using other algorithms, and our results can be directly compared with theirs. In two dimensions we carry out a relativistic extension of Emery's step test, a benchmark for numerical schemes in classical hydrodynamics and an astrophysical application, the evolution of a relativistic jet moving at a supersonic speed. Finally, we draw some conclusions in Section 6.

2. HRSC METHODS IN RFD

In recent years, and trailing the evolution of computational methods for classical fluid dynamics, several new methods for numerical RFD have been designed which exploit the hyperbolic and conservative character of the relativistic equations.

The first step toward the adaptation of HRSC techniques to RFD consists in rewriting the system of Eqs. (1) in conservation (or *divergence*) form:

$$\partial_t \mathbf{u} + \nabla \cdot \mathbf{f}(\mathbf{u}) = \mathbf{0}. \tag{4}$$

This basic step serves to identify the set of unknowns, the vector of *conserved quantities* $\mathbf{u}$, and their corresponding fluxes $\mathbf{f}(\mathbf{u})$. Once the equations have been written in conservation form, almost every high resolution method devised to solve hyperbolic systems of conservation laws can be extended to RFD.

To focus our discussion, we shall restrict our attention to special relativistic hydrodynamics. In this case and for a perfect gas, system (1) can be rewritten as (see [12])

$$\frac{\partial \mathbf{F}^{\mu}(\mathbf{w})}{\partial x^{\mu}} = 0, \tag{5}$$

with

$$\mathbf{w} = (\rho, v^i, \varepsilon)^T \tag{6}$$

$$\mathbf{F}^0(\mathbf{w}) = (\rho W, \rho h W^2 v^j, \rho h W^2 - p - \rho W)^T \tag{7}$$

$$\mathbf{F}^i(\mathbf{w}) = (\rho W v^i, \rho h W^2 v^j v^i + p\delta^{ij}, \rho h W^2 v^i - \rho W v^i)^T. \tag{8}$$

Here $x^{\mu} = (t, x, y, z)$ and $v^i = U^i/W$ with ρ, h, ϵ, p, and U^i are as defined in Section 1, and W, the Lorentz factor ($W \equiv U^0$), satisfies $W = (1 - \mathrm{v}^2)^{-1/2}$, with $\mathrm{v}^2 = \delta_{ij} v^i v^j$.

We consider the variables

$$\begin{aligned} D &= \rho W \\ S^j &= \rho h W^2 v^j \\ \tau &= \rho h W^2 - p - \rho W, \end{aligned} \tag{9}$$

which are, respectively, the rest-mass, momentum, and total energy densities, measured in the laboratory frame. Then, defining the vector of conserved quantities as

$$\mathbf{u} = (D, S^j, \tau), \tag{10}$$

system (5) takes the required *conservative form*:

$$\frac{\partial \mathbf{u}}{\partial t} + \sum_i \frac{\partial \mathbf{f}^i(\mathbf{u})}{\partial x_i} = 0. \tag{11}$$

Written in this form, the hyperbolic character of the RFD system is explicitly displayed in a form that is suitable for the application of the HRSC machinery developed in classical gas dynamics.

The system of partial differential equations is closed, as usual, with an equation of state $p = p(\rho, \varepsilon)$. Anile [1] has shown that system (10)–(11) is hyperbolic for causal equations of state, i.e., those satisfying $c_s < 1$, where c_s, defined as

$$h c_s^2 = \frac{\partial p}{\partial \rho} + (p/\rho^2)\frac{\partial p}{\partial \epsilon}, \tag{12}$$

is the local sound velocity.

When applying a shock capturing technique to a conservative formulation of system (1), the code evolves the conserved quantities in time. The local rest-frame variables $\{\rho, \epsilon, p\}$ and the three-velocity v^j have to be computed at least once per time step in each computational cell. This computation requires a nonlinear root-finding routine [19].

Modern HRSC schemes use the characteristic structure of the hyperbolic system of conservation laws. In many Godunov-type schemes, the characteristic structure is used to compute either an exact or an approximate solution to a sequence of Riemann problems at each cell interface. In characteristic based methods (see [10] or [27]), the characteristic

structure is used to compute the local characteristic fields, which, in the case of a system, are the quantities that are properly thought of as propagating in various directions.

In each of these two approaches, the characteristic decomposition of the Jacobian matrices of the nonlinear system of conservation laws is important, not only because it is one of the key ingredients in the design of the numerical flux at the interfaces, but because experience has shown that it facilitates a robust upgrading of the order of a numerical scheme.

Following a procedure similar to the one described in [12], we have derived analytical expressions for the spectral decomposition of the three 5×5 Jacobian matrices $\mathcal{B}^i(\mathbf{u})$ associated with the fluxes $\mathbf{f}^i(\mathbf{u})$ of system (10)–(11),

$$\mathcal{B}^i(\mathbf{u}) = \frac{\partial \mathbf{f}^i(\mathbf{u})}{\partial \mathbf{u}}. \tag{13}$$

The eigenvalues of matrix $\mathcal{B}^x(\mathbf{u})$ are (the $i = y, z$ cases are easily obtained by symmetry):

$$\lambda_\pm = \frac{1}{1 - \mathrm{v}^2 c_s^2}\left\{ v^x\left(1 - c_s^2\right) \pm c_s \sqrt{(1 - \mathrm{v}^2)\left[1 - v^x v^x - (\mathrm{v}^2 - v^x v^x)c_S^2\right]}\right\}, \tag{14}$$

$$\lambda_0 = v^x \quad \text{(triple)}. \tag{15}$$

To give the expression of the right and left eigenvectors, we define the auxiliary quantities

$$\mathcal{K} \equiv \frac{\tilde{\kappa}}{\tilde{\kappa} - c_s^2}, \quad \mathcal{A}_\pm \equiv \frac{1 - v^x v^x}{1 - v^x \lambda_\pm} \tag{16}$$

with

$$\tilde{\kappa} = \frac{1}{\rho}\frac{\partial p}{\partial \epsilon}$$

computed from the equation of state.

A complete set of *right-eigenvectors* is

$$\mathbf{r}_{0,1} = \left(\frac{\mathcal{K}}{hW}, v^x, v^y, v^z, 1 - \frac{\mathcal{K}}{hW}\right) \tag{17}$$

$$\mathbf{r}_{0,2} = (Wv^y, 2hW^2 v^x v^y, h(1 + 2W^2 v^y v^y), 2hW^2 v^y v^z, 2hW^2 v^y - Wv^y) \tag{18}$$

$$\mathbf{r}_{0,3} = (Wv^z, 2hW^2 v^x v^z, 2hW^2 v^y v^z, h(1 + 2W^2 v^z v^z), 2hW^2 v^z - Wv^z) \tag{19}$$

$$\mathbf{r}_\pm = (1, hW\mathcal{A}_\pm \lambda_\pm, hWv^y, hWv^z, hW\mathcal{A}_\pm - 1). \tag{20}$$

The corresponding complete set of *left-eigenvectors* is

$$\mathbf{l}_{0,1} = \frac{W}{\mathcal{K} - 1}(h - W, Wv^x, Wv^y, Wv^z, -W)$$

$$\mathbf{l}_{0,2} = \frac{1}{h(1 - v^x v^x)}(-v^y, v^x v^y, 1 - v^x v^x, 0, -v^y)$$

$$\mathbf{l}_{0,3} = \frac{1}{h(1 - v^x v^x)}(-v^z, v^x v^z, 0, 1 - v^x v^x, -v^z)$$

$$\mathbf{l}_{\mp} = (\pm 1)\frac{h^2}{\Delta}\begin{bmatrix} hW\mathcal{A}_{\pm}(v^x - \lambda_{\pm}) - v^x - W^2(\mathrm{v}^2 - v^x v^x)(2\mathcal{K}-1)(v^x - \mathcal{A}_{\pm}\lambda_{\pm}) + \mathcal{K}\mathcal{A}_{\pm}\lambda_{\pm} \\ 1 + W^2(\mathrm{v}^2 - v^x v^x)(2\mathcal{K}-1)(1-\mathcal{A}_{\pm}) - \mathcal{K}\mathcal{A}_{\pm} \\ W^2 v^y (2\mathcal{K}-1)\mathcal{A}_{\pm}(v^x - \lambda_{\pm}) \\ W^2 v^z (2\mathcal{K}-1)\mathcal{A}_{\pm}(v^x - \lambda_{\pm}) \\ -v^x - W^2(\mathrm{v}^2 - v^x v^x)(2\mathcal{K}-1)(v^x - \mathcal{A}_{\pm}\lambda_{\pm}) + \mathcal{K}\mathcal{A}_{\pm}\lambda_{\pm} \end{bmatrix},$$

where Δ is the determinant of the matrix of right-eigenvectors:

$$\Delta = h^3 W(\mathcal{K}-1)(1 - v^x v^x)(\mathcal{A}_+\lambda_+ - \mathcal{A}_-\lambda_-). \tag{21}$$

For an ideal gas equation of state, $\mathcal{K} = h$; thus, $\mathcal{K} > 1$ and Δ is different from zero ($|v^x| < 1$).

In a previous work [12], the algebraic study of the characteristic fields was restricted to find the eigenvalues and right-eigenvectors of the Jacobian matrices of system (5). Hence, a multiplication of the right-eigenvectors matrix by the Jacobian matrix associated to the flux in the temporal direction of system (5) was necessary. Besides that incomplete analysis, the code in [12] also included a time-consuming matrix-inversion routine for the computation of the left-eigenvectors. The procedure, albeit rudimentary, allowed the construction of a two-dimensional code that was able to successfully simulate mildly relativistic flows in two dimensions.

We would like to point out that, to the best of our knowledge, this is the first time that a full, ready-to-implement description of the characteristic structure of system (11) in multidimensions is explicitly given. This spectral decomposition provides the user with the technical ingredients needed to develop state-of-the-art, upwind-biased HRSC codes for numerical relativistic hydrodynamics in a way which is identical to the classical case. Let us note, however, that the characteristic wave speeds in the relativistic case not only depend on the fluid velocity components in the wave propagation direction, but also on the normal velocity components. This coupling adds new numerical difficulties which are specific to RFD.

3. MARQUINA'S SCHEME

In [4] Donat and Marquina propose a new flux formula to compute the numerical flux at a cell interface.

In the scalar case Marquina's flux formula is precisely an entropy satisfying numerical flux formula used by Shu and Osher in the design of their ENO schemes [27]. The novelty of the approach described in [4] lies in the extension of Shu–Osher's numerical flux to systems of hyperbolic conservation laws. In Marquina's scheme there are no Riemann solutions involved (either exact or approximate) and there are no artificial intermediate states constructed at each cell interface.

Given the spectral decompositions described in Section 2, the implementation of Marquina's scheme in RFD is straightforward; we simply follow the recipe described in [4] to obtain the first-order scheme. For the sake of completeness, we shall include the basic description of the first-order scheme in the one-dimensional case.

To compute the numerical flux at a given interface, separating the states $\mathbf{u_l}$ and $\mathbf{u_r}$, we compute first the *sided* local characteristic variables and fluxes:

$$\omega_l^p = \mathbf{l}^p(\mathbf{u_l}) \cdot \mathbf{u_l}, \quad \phi_l^p = \mathbf{l}^p(\mathbf{u_l}) \cdot \mathbf{f}(\mathbf{u_l}),$$
$$\omega_r^p = \mathbf{l}^p(\mathbf{u_r}) \cdot \mathbf{u_r}, \quad \phi_r^p = \mathbf{l}^p(\mathbf{u_r}) \cdot \mathbf{f}(\mathbf{u_r}).$$

Here $\mathbf{l}^p(\mathbf{u_l}), \mathbf{l}^p(\mathbf{u_r})$ for $p = 1, 2 \ldots, m$ are the (normalized) left eigenvectors of the Jacobian matrices $\mathcal{B}(\mathbf{u_l}), \mathcal{B}(\mathbf{u_r})$. Let $\lambda_p(\mathbf{u_l}), \lambda_p(\mathbf{u_r}),\ p = 1, 2 \ldots, m$, be their corresponding eigenvalues. We proceed as follows:

For $k = 1, \ldots, m$

If $\lambda_k(\mathbf{u})$ does not change sign in $[\mathbf{u_l}, \mathbf{u_r}]$, then

If $\lambda_k(\mathbf{u_l}) > 0$ then

$$\phi_+^k = \phi_l^k$$
$$\phi_-^k = 0$$

else

$$\phi_+^k = 0$$
$$\phi_-^k = \phi_r^k$$

endif

else

$$\alpha_k = \max_{\mathbf{u} \in \Gamma(\mathbf{u_l}, \mathbf{u_r})} |\lambda_k(\mathbf{u})|$$
$$\phi_+^k = .5 \cdot \left(\phi_l^k + \alpha_k \omega_l^k\right)$$
$$\phi_-^k = .5 \cdot \left(\phi_r^k - \alpha_k \omega_r^k\right)$$

endif

$\Gamma(\mathbf{u_l}, \mathbf{u_r})$ is a curve in the space of states of the system connecting $\mathbf{u_l}$ and $\mathbf{u_r}$. For any hyperbolic system where the fields are either genuinely nonlinear or linearly degenerate, we can test the possible sign changes of $\lambda_k(\mathbf{u})$ by checking the sign of $\lambda_k(\mathbf{u_l}) \cdot \lambda_k(\mathbf{u_r})$. Also, α_k can be determined as

$$\alpha_k = \max\{|\lambda_k(\mathbf{u_l})|, |\lambda_k(\mathbf{u_r})|\}.$$

The numerical flux that corresponds to the cell-interface separating the states $\mathbf{u_l}$ and $\mathbf{u_r}$ is then

$$\mathbf{F}^M(\mathbf{u_l}, \mathbf{u_r}) = \sum_{p=1}^{m} \left(\phi_+^p \mathbf{r}^p(\mathbf{u_l}) + \phi_-^p \mathbf{r}^p(\mathbf{u_r})\right). \tag{22}$$

Marquina's scheme can thus be interpreted as a characteristic-based scheme that avoids the use of an *averaged* intermediate state to perform the transformation to the local characteristic fields. The common approach in all characteristic-based methods is to evaluate this transformation at some reasonable average of the states adjacent to each cell interface. There is clearly a great deal of ambiguity in choosing this average (as opposed to what happens in the approximate Riemann solver context) and any particular choice seems to introduce subtle spurious features into the solution. In Marquina's scheme the ambiguity is avoided by using directly the unambiguous data on the left and right sides of each cell wall.

The extension to higher dimensions is accomplished, as in [27], in a dimension by dimension fashion, so that the one-dimensional method applies unchanged to higher dimensional problems.

To construct higher order versions of the scheme, we follow the *method of lines* approach (see, e.g., [14]). We consider the discretization process in two stages, discretizing first only in space, leaving the problem continuous in time. This step leads to a system of ordinary differential equations in time, called the "semi-discrete equations." We then discretize in time using any standard numerical ODE solver.

This simple procedure decouples the time and space discretizations. High order accuracy in space can be achieved by applying a high order interpolation procedure in space, while

high order accuracy in time is obtained by applying an adequate high order ODE solver. This approach is also particularly useful in extending methods to two or more space dimensions.

In this paper we choose to follow the simplified ENO framework of Shu and Osher [27] to improve the order of the method. Shu–Osher numerical schemes have been already used in RFD. In [15] a numerical scheme of this type was used to simulate ultrarelativistic one-dimensional flows. Later on, Dolezal and Wong [6] have also applied the techniques in [27] to collisions of heavy ions.

In this framework the spatial order of accuracy is improved by performing an upwind biased ENO type reconstruction on the characteristic fluxes. The time evolution step is carried out by a family of Runge–Kutta methods which are also total variation diminishing (see [27] for details).

In the context of Marquina's scheme, we perform the reconstruction procedure on the characteristic fluxes ϕ_l^p, ϕ_r^p, which are constructed using the spectral information of the Jacobian matrices $\mathcal{B}(\mathbf{u_l})$ and $\mathcal{B}(\mathbf{u_r})$. The states $\mathbf{u_l}$ and $\mathbf{u_r}$ on both sides of a cell boundary are computed using the same type of reconstruction procedure as for the characteristic fluxes.

Higher order versions of Marquina's scheme lead to full HRSC schemes, i.e., schemes with sharp resolution at discontinuities, no spurious oscillatory behavior, and at least second-order accuracy in smooth regions of the flow.

Technical remarks. In this paper we shall consider second- and third-order extensions of Marquina's scheme. In our numerical experimentation (both in the classical and relativistic frameworks) we have observed that the piecewise-hyperbolic reconstruction (PHM [16]) is slightly more robust in many situations (probably because it is more local than the ENO parabolic reconstruction) and it is therefore our preferred third-order reconstruction.

An extensive comparison between the third-order reconstructions available in the literature is presently under way; however, in general terms we can say that the second-order reconstructions are more robust under extreme circumstances than the third-order ones (PHM and ENO3). We shall be more specific in each example within the next section.

In carrying out Marquina's scheme, we have to compute $\mathcal{B}(\mathbf{u_l})$ and $\mathcal{B}(\mathbf{u_r})$ at each cell interface. In the first-order method, at the boundary between the jth and the $(j+1)$th cell we have $\mathbf{u_l} = \mathbf{u}_j$ and $\mathbf{u_r} = \mathbf{u}_{j+1}$; thus we only need to carry out one Jacobian evaluation per cell-interface, which is exactly the same computational effort required in a numerical scheme based on a Roe-like approximate Riemann solver. However, in a high order extension we have to compute the left and right states $\mathbf{u_l}, \mathbf{u_r}$ using an appropriate reconstruction procedure. This leads to *two* Jacobian evaluations per cell-interface, instead of one, and, thus, to an increase in the computational cost of the method.

In the original formulation (see [4]), the reconstruction step is performed on the conserved variables, but doing this in RFD increases the computational cost, since it becomes necessary to return to the rest-frame quantities in order to complete the computation of the spectral decompositions. To minimize the computational cost in our codes, the reconstruction step in the upgrading process is done directly on ρ, v^i, and ε; then p and h are computed from the equation of state and (3), respectively.

4. ONE-DIMENSIONAL NUMERICAL EXPERIMENTS

Riemann problems involving flow in a constant section pipe have become standard test problems in numerical hydrodynamics. The flow evolution involves shock and rarefaction waves, as well as contact discontinuities, and can be computed analytically in a way which is

similar to the classical case [18]. The comparison of the numerical approximations obtained by a given algorithm and the true solution provides thus a good measurement of its efficiency and accuracy.

In this section we apply our codes to several one-dimensional flows of the above type moving at relativistic velocities. All of them have been considered by other authors [19, 23, 26] and their results can be compared with ours.

4.1. *Relativistic Blast Wave Tests*

The original setup of these test problems is as follows: At time $t = 0$ two regions of an ideal gas at rest with pressures p_L and p_R and densities ρ_L and ρ_R are separated by a diaphragm which is suddenly removed. As in the nonrelativistic case, four constant states occur, separated by three elementary waves; details on the exact solution can be found in [18, 26]. The main differences between the solution of relativistic shock tubes and their Newtonian counterparts are due to the nonlinear velocity addition and the Lorentz contraction. The first effect yields a curved profile for the rarefaction fan, as opposed to a linear one in the Newtonian case. The Lorentz contraction narrows the shock plateau. These effects, especially the second one, become particularly strong in the ultrarelativistic regime.

We have simulated two particular shock tube tests for which the solution consists of a rarefaction wave traveling to the left and a shock wave moving to the right, with a contact discontinuity in between. The initial states are as follows:

Case 1. $\{p_L = 13.3,\ \rho_L = 10,\ v_L = 0\}$, $\{p_R = 0,\ \rho_R = 1,\ v_R = 0\}$;

Case 2. $\{p_L = 10^3,\ \rho_L = 1,\ v_L = 0\}$, $\{p_R = 10^{-2},\ \rho_R = 1,\ v_R = 0\}$.

In our numerical experiments the computational domain is [0, 1] and, at $t = 0$, the diaphragm is placed at $x = 0.5$. We use an ideal gas law, $p = (\Gamma - 1)\rho\epsilon$ with $\Gamma = 5/3$. In Case 1 and for numerical reasons, the pressure of the right state has been set to a small finite value ($p_R = 0.66 \times 10^{-6}$).

Case 1. Figures 1–3 show the normalized profiles of pressure, density, and velocity, obtained with our first-, second-, and third-order codes (labeled "Plain," "ENO2," and "ENO3," respectively), at time $t = 0.4$ on an Eulerian grid of 200 zones. This allows for a direct comparison with the results in [26]. By this time the exact solution (continuous line) has a fully developed structure. The leading shock is placed at $x = 0.83$, the trailing contact discontinuity at $x = 0.78$, and the corners of the rarefaction profile are located at $x = 0.21$ and $x = 0.56$. The velocity of the gas behind the shock reaches the value of 0.72 and the relativistic effects are already noticeable. It can be seen that our second- and third-order extensions display no spurious overshoots or undershoots at rarefaction wave corners.

The numerical solution obtained with our first-order code shows an $O(\Delta x)$ kink in the rarefaction wave profile. This pathology, well known in Newtonian first-order codes, disappears in our higher order numerical approximations. It is observed in these figures that the obtained profiles are sharper and the overall resolution improves as the order of the method increases.

Figure 4 shows a third-order approximation on a 400 zones grid. The results show that the quality of the computed solution is similar to the one obtained by Martí and Müller in [19] with a relativistic extension of the PPM method which employs the *exact* relativistic Riemann solver.

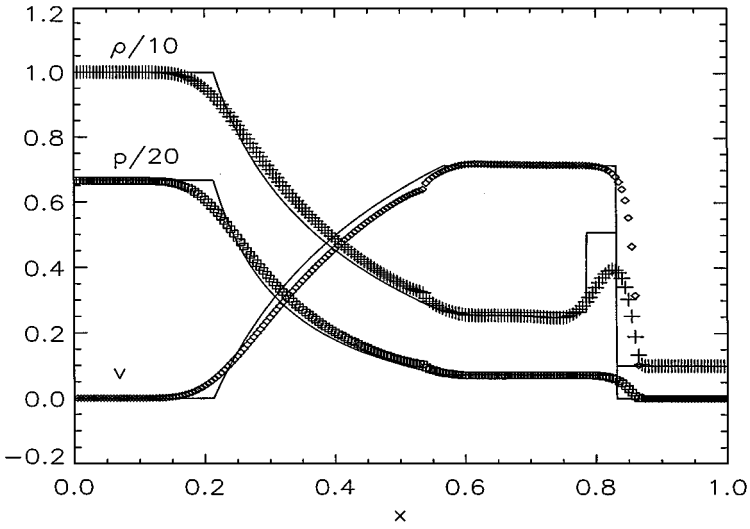

FIG. 1. The relativistic blast wave problem 1 for time $t = 0.4$. Normalized profiles of density, pressure and velocity vs distance for the computed and exact (solid line) solution. All variables were calculated with a first-order scheme (plain) on an equidistant grid of 200 zones.

Table 1 displays the mean errors for the three methods. The largest errors occur in the postshock area. In a smooth region, such as the curved profile of the rarefaction wave, the errors are much smaller. For example, for the 200 zones runs, there is only a 7.09%, 3.12%, 2.37% error in the first-, second-, and third-order approximations to the density, respectively. In the 400 zones run, the error in the third-order approximation is reduced to 1.18%.

We should also mention that, in this particular problem, the third-order PHM reconstruction (which uses hyperbolae as reconstructing functions) leads to negative internal energies,

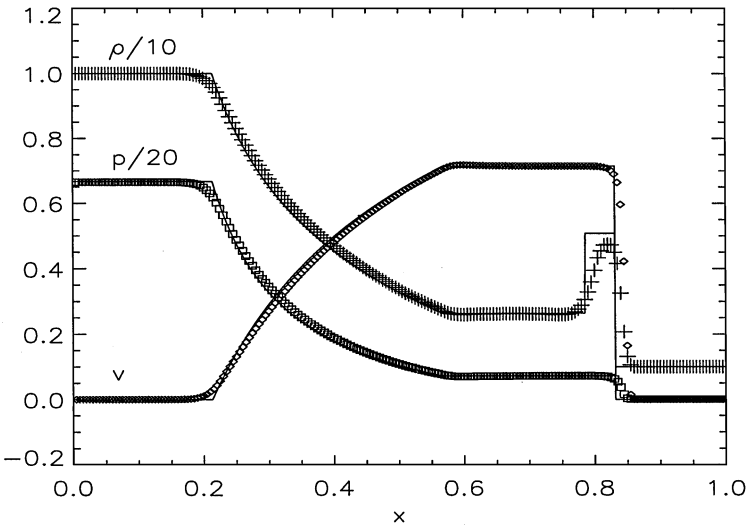

FIG. 2. The relativistic blast wave problem 1 for time $t = 0.4$. Normalized profiles of density, pressure and velocity vs distance for the computed and exact (solid line) solution. All variables were calculated with a second-order scheme (ENO2) on an equidistant grid of 200 zones.

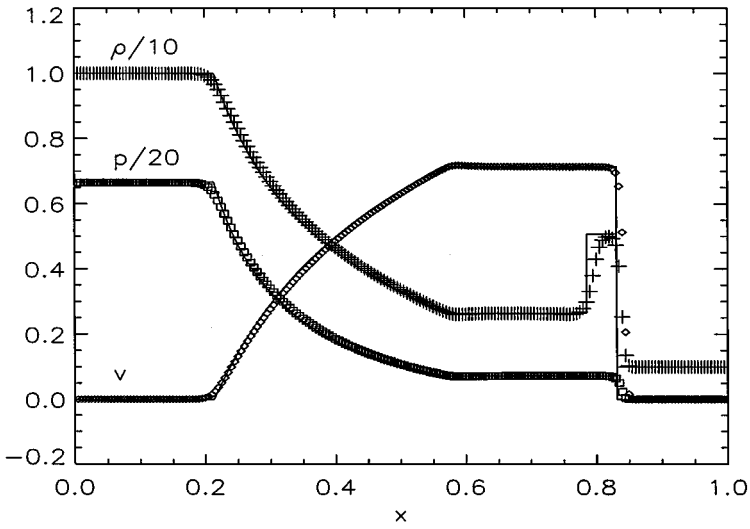

FIG. 3. The relativistic blast wave problem 1 for time $t = 0.4$. Normalized profiles of density, pressure, and velocity vs distance for the computed and exact (solid line) solution. All variables were calculated with a third-order scheme (ENO3) on an equidistant grid of 200 zones.

which causes the code to crash. This trend appears whenever there are large jumps into cold regions ($p \to 0$). A common practice in this situation, which we shall not follow in this paper, is to substitute these negative values (which are in fact very small) by positive ones. This simple procedure leads, however, to a loss of conservation.

Case 2. This test was first considered by Norman and Winkler [23]. The flow pattern is similar to that of Case 1 but the relativistic effects make it much more severe.

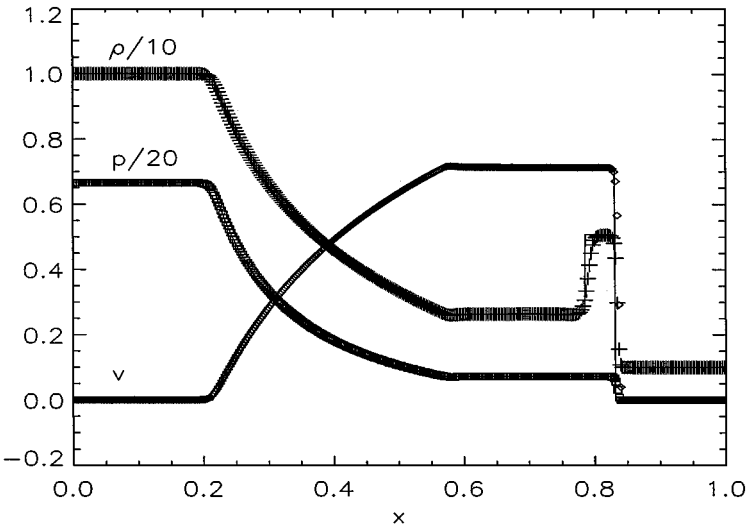

FIG. 4. The relativistic blast wave problem 1 for time $t = 0.4$. Normalized profiles of density, pressure and velocity vs distance for the computed and exact (solid line) solution. All variables were calculated with a third-order scheme (ENO3) on an equidistant grid of 400 zones.

TABLE 1
L-1 Norm Errors of Density, Velocity, and Pressure for the Relativistic Blast Wave Problems

Case	Scheme	Δx	$\|E(\rho)\|_1$	$\|E(v)\|_1$	$\|E(p)\|_1$
1	Plain	$\frac{1}{200}$	$2.83E-01$	$3.16E-02$	$2.52E-01$
	ENO2		$1.35E-01$	$1.54E-02$	$1.06E-01$
	ENO3		$9.70E-02$	$1.15E-02$	$7.77E-02$
	ENO3	$\frac{1}{400}$	$5.35E-02$	$6.26E-03$	$4.24E-02$
2	Plain	$\frac{1}{400}$	$1.86E-01$	$5.75E-02$	$1.34E+01$
	ENO2		$1.54E-01$	$2.64E-02$	$4.91E-00$
	PHM		$1.12E-01$	$1.68E-02$	$3.09E-00$

Note. The second column displays the reconstruction procedure used.

An initial jump in pressure of five orders of magnitude leads to the formation of a thin and dense shell bounded by a leading shock front and a trailing contact discontinuity. The postshock velocity is 0.96 ($W \approx 3.5$), while the shock speed is 0.986 ($W \approx 6$).

The thin shock plateau is a hard test for any numerical scheme. Norman and Winkler [23], with an implicit hydrodynamical code that incorporated artificial-viscosity terms, had to use an adaptive grid to obtain consistent profiles. Conservative methods do a good job with a fixed Eulerian grid. Martí and Müller, with their relativistic PPM, obtain in [19] results comparable to those of [23] with a fixed Eulerian grid and an explicit numerical code.

Figures 5–7 show our numerical results. We use an Eulerian grid of 400 zones to allow for a direct comparison with [19]. As in Case 1, our third-order method gives the same overall resolution as their relativistic PPM with the exact Riemann solver.

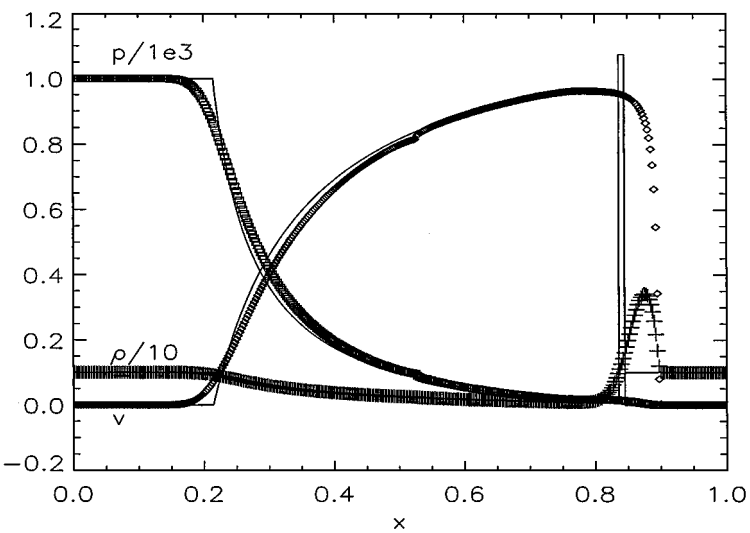

FIG. 5. The relativistic blast wave problem 2 for time $t = 0.35$. Normalized profiles of density, pressure and velocity vs distance for the computed and exact (solid line) solution. All variables were calculated with a first order scheme (plain) on an equidistant grid of 400 zones.

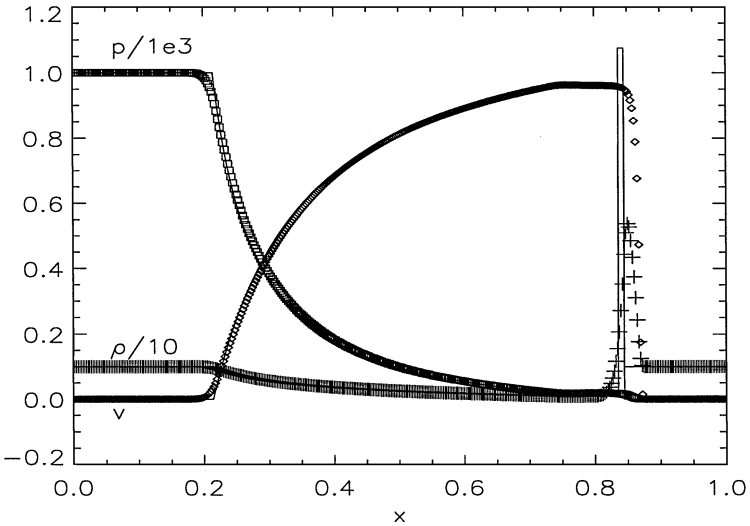

FIG. 6. The relativistic blast wave problem 2 for time $t = 0.35$. Normalized profiles of density, pressure and velocity vs distance for the computed and exact (solid line) solution. All variables were calculated with a second order scheme (ENO2) on an equidistant grid of 400 zones.

Table 1 displays the mean errors for the three methods. As in Case 1 (and also as in [19]), the largest errors occur in the postshock area. In a smooth region, such as the curved profile of the rarefaction wave, there is only a 0.52%, 0.19%, 0.11% error in the first-, second-, and third-order approximations to the density, respectively.

It is worth mentioning that the ENO third-order reconstruction leads, in this problem, to velocities greater than one, the speed of light, causing the code to crash. On the other hand and because the jump in pressure does not involve a *cold* gas, the PHM reconstruction leads to a well-behaved numerical approximation which is *formally* third-order accurate.

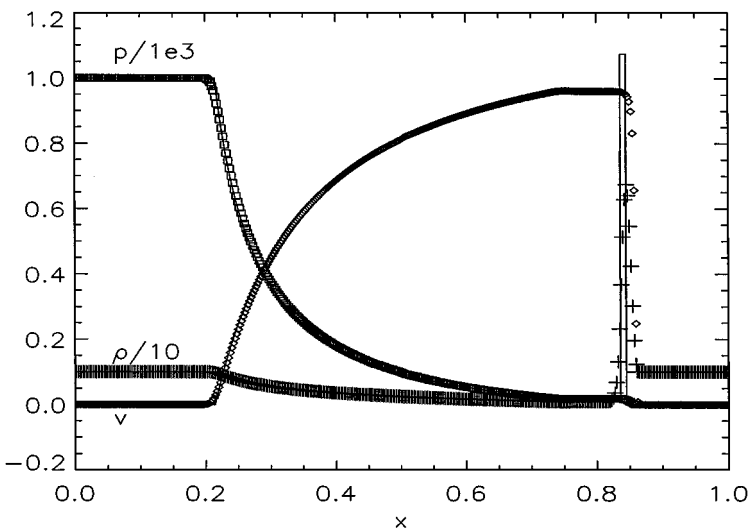

FIG. 7. The relativistic blast wave problem 2 for time $t = 0.35$. Normalized profiles of density, pressure and velocity vs distance for the computed and exact (solid line) solution. All variables were calculated with a third-order scheme (PHM) on an equidistant grid of 400 zones.

4.2. *Relativistic Shock Reflection Test*

An ideal cold gas ($\epsilon_1 = 0$) with velocity v_1 hits a wall. The gas is thus compressed and heated, giving rise to a shock which starts to propagate off the wall, leaving the gas behind at rest ($v_2 = 0$). Subscripts 1 and 2 stand for the states of gas ahead and behind, respectively, of the shock.

The postshock density is an increasing function of the initial inflow velocity according to the compression ratio σ ($\equiv \rho_2/\rho_1$),

$$\sigma = \frac{\Gamma + 1}{\Gamma - 1} + \frac{\Gamma}{\Gamma - 1}\epsilon_2, \tag{23}$$

where $\epsilon_2 = W_1 - 1$ and Γ is the adiabatic index of the equation of sate. As is well known, in the Newtonian limit this compression ratio is independent of the initial velocity. On the contrary, in the ultrarelativistic regime the density of the gas behind the shock is unbounded ($\sigma \sim W_1$).

In our numerical setup the computational domain covers the interval [0, 1] and the wall is placed at $x = 1$. We use an Eulerian grid of 100 zones and an ideal gas with $\Gamma = 5/3$. For numerical reasons, the specific internal energy of the inflow gas was set to a small initial value ($\varepsilon_1 = 10^{-5} W_1$).

Figure 8 shows the normalized profiles of the pressure, density, and velocity obtained with our ENO2 code at a time when the shock has propagated 0.5 units off the wall. The profiles shown correspond to an initial velocity $v_1 = 0.99999$ ($W \approx 224$). As in the previous tests, the shock resolution is poorer in the numerical profiles, corresponding to the first-order method (not shown). The inflow velocity imposes no particular theoretical or numerical constraints on the scheme, which means that the ultrarelativistic regime poses no special difficulties in the simulations. Different runs varying the inflow velocity (not shown) gave qualitatively similar profiles.

There are, however, several technical remarks that need to be pointed out:

Because the numerical simulation involves a cold gas, the PHM reconstruction may cause a code-crash in the case of extremely large pressure jumps when negative values of the

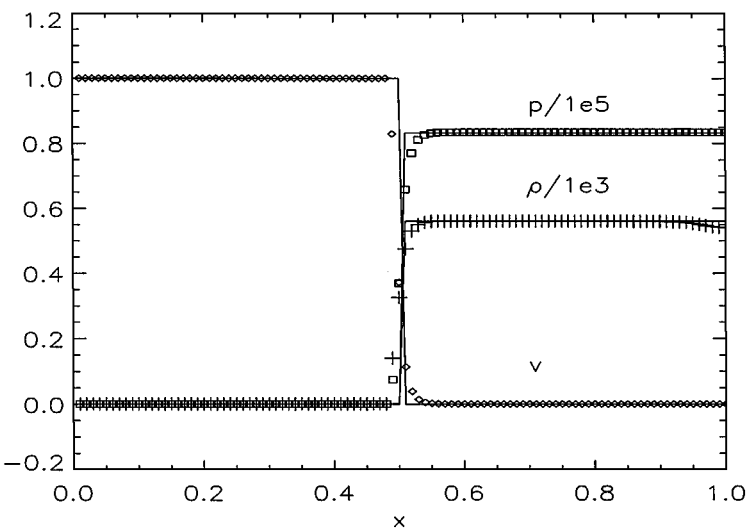

FIG. 8. The relativistic shock reflection problem for a time when the shock has propagated 0.5 units off the wall: normalized profiles of density, pressure, and velocity vs distance for the computed and exact (solid line) solution. All variables were calculated with a second-order (ENO2) approximation on an equidistant grid of 100 zones.

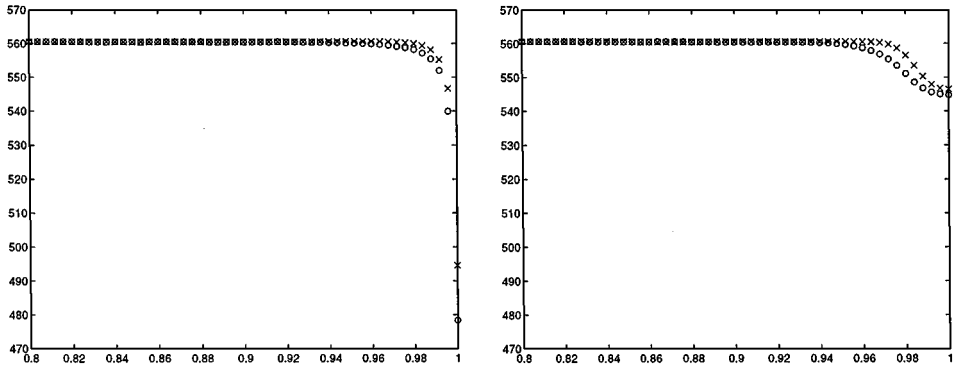

FIG. 9. Relativistic shock reflection test: unnormalized density profile 50 zones next to the right wall on a 250-zone grid. Left: Shu–Osher scheme. Right: Marquina's scheme. x, PHM; o, ENO2.

internal energy may be obtained. The problem usually disappears when we increase the spatial resolution (which in turn, increases the resolution power of the numerical reconstruction procedure). In this problem, we obtain a well-behaved numerical approximation with a PHM-third-order code and 250 zones in the computational domain (see Fig. 9).

In treating extremely large velocities ($v \approx 1$) we will eventually hit the numerical precision barrier, when the velocity becomes numerically indistinguishable from unity, or even (because of the essentially non-oscillatory character of the reconstruction procedures considered in this paper) the reconstructed velocities may become slightly larger than one, causing the code to crash. A remedy for this extreme situation consists of carrying out the reconstruction procedure on the spatial components of the 4-velocity $U^j = v^j W$; defining $U^2 = \delta_{ij} U^i U^j$ we then have $W = (1+U^2)^{1/2}$. This can be included in the original formulation of the conservative form of the scheme [8] or incorporated into the existing formulation [6]. The numerical test in Figs. 8 and 9 have been done including the second option in the basic scheme.

At the shock location, the numerical procedure described in [19] to recover the values of the rest-frame quantities from the conserved variables becomes quite inefficient for large values of the inflow velocity. This is due to the extremely large pressure jumps and the poor choice of the initial pressure in the root-finding routine. Typically, the maximum number of Newton–Raphson iterations is 3–4, and this is the case, in this problem, for inflow velocities up to $1-10^{-9}$ (i.e., $W_1 > 2 \times 10^4$; in any case, well above the range needed in applications), this value increases up to 30–40 for $v_1 = 1 - 10^{-10}$ and up to 300–400 for $v_1 = 1 - 10^{-11}$. However, the deficiency can be easily overcome by taking an appropriate average of various neighboring pressure values as the initial guess for the Newton–Raphson iteration.

Conventional schemes applied to shock reflection tests often give numerical approximations with a consistent $O(1)$ error in the density and internal energy in a few cells near the reflecting wall. This "overheating," as it is known in classical hydrodynamics (see, e.g., [4] and references therein), is purely a numerical artifact which is considerably reduced when Marquina's scheme is used. This was the case in classical gas dynamics simulations (see [4]) and it also seems to apply to RFD simulations. For the sake of comparison, the left side of Fig. 9 displays the numerical values obtained with Shu–Osher's scheme at the last 50 zones near the wall (at $x = 1$), with several reconstruction procedures on a 250-zone grid. The "overheating" phenomenon is clearly visible and it leads to a 17% error at the wall in the first-order scheme (11% in its PHM version). The right side of the same figure displays

the numerical values obtained with Marquina's scheme. In this case the error at the wall is less than 4% in the first order version of Marquina's scheme (around 2.5% in its PHM version). As in the classical gas dynamics case, Marquina's scheme seems to be able to reduce the "wall heating error" in shock reflection problems.

5. MULTIDIMENSIONAL NUMERICAL EXPERIMENTS

5.1. *Wind Tunnel with a Flat-Faced Step*

A challenging test for two-dimensional shock calculations is the numerical simulation of a wind tunnel with a flat-faced step, originally introduced by Emery [7] to compare several difference schemes in classical fluid dynamics. We have extended this test to the relativistic (and ultrarelativistic) flow regime, trying to keep the geometry and most of the initial conditions as in the original experiment [7].

A Mach 3 flow (Newtonian definition) is injected into a tunnel containing a step. The tunnel is three units long and one unit wide. The step is 0.2 units high and it is located 0.6 units from the left-hand end of the tunnel. Initially, the wind tunnel is filled with an ideal gas with $\Gamma = 7/5$, which everywhere has density $\rho(0, x, y) = \rho_0 = 1.4$, $v^x(0, x, y) = v_0^x$, and $v^y(0, x, y) = v_0^y = 0$ for all x, y. Gas with these properties is continually fed in from the left-hand boundary.

An inflow boundary condition is applied at the left end of the computational domain and outflow boundary conditions are applied at the right end. Along the walls of the tunnel, as well as on the boundary marked by the step, reflecting boundary conditions are applied. The corner of the step is the center of a rarefaction fan and, thus, a singular point of the flow. As in the classical gas dynamics framework [33], numerical errors generated in the neighborhood of this point can seriously affect the global flow. Our experimentation confirms that, just as in the Newtonian limit, it is necessary to apply an additional boundary condition near the corner of the step in order to minimize the generation of numerical errors near this singular point. Our corner treatment is based on a relativistic extension of the conditions imposed in [33] for Newtonian gas dynamics. Specific details can be found in the Appendix.

The computational domain is discretized using a rectangular grid of 120 x-cells $\times$ 40 y-cells. The initial value of the x-component of the three velocity, v_0^x, has been used as a free parameter for different runs. For our ENO2 method, the computational time per cell and time step on an Apollo 9000 712/100 is 2×10^{-3} seconds. For the plain method the computational time per cell and time step on the same machine is 0.7×10^{-3}.

The density distribution is the hardest one to compute due, on one hand, to the Mach stem at the upper wall and, on the other hand, to the corner of the step. Moreover, in the ultrarelativistic regime where the Lorentz factor $W \gg 1$, the large jumps in density and pressure make the test much more severe. The general evolution is similar to the Newtonian case (see [33]) but the bow shock moves much faster in the ultrarelativistic regime. In the computational domain we consider, an overall steady flow never develops and eventually the bow shock leaves the computational domain. The exit time depends on the inflow velocity.

Figure 10 shows contour plots of the density obtained with our first-, second-, and third-order codes for $v_0^x = 0.995$, which corresponds to $W \approx 10$. By time $t = 4.3$ the unsteady flow has a rich and interesting structure. The location of the bow shock, Mach stem, and reflected shock are consistent in the three runs. As in the one-dimensional case, increasing the order of the method leads to sharper profiles, i.e., less numerical viscosity. This is especially

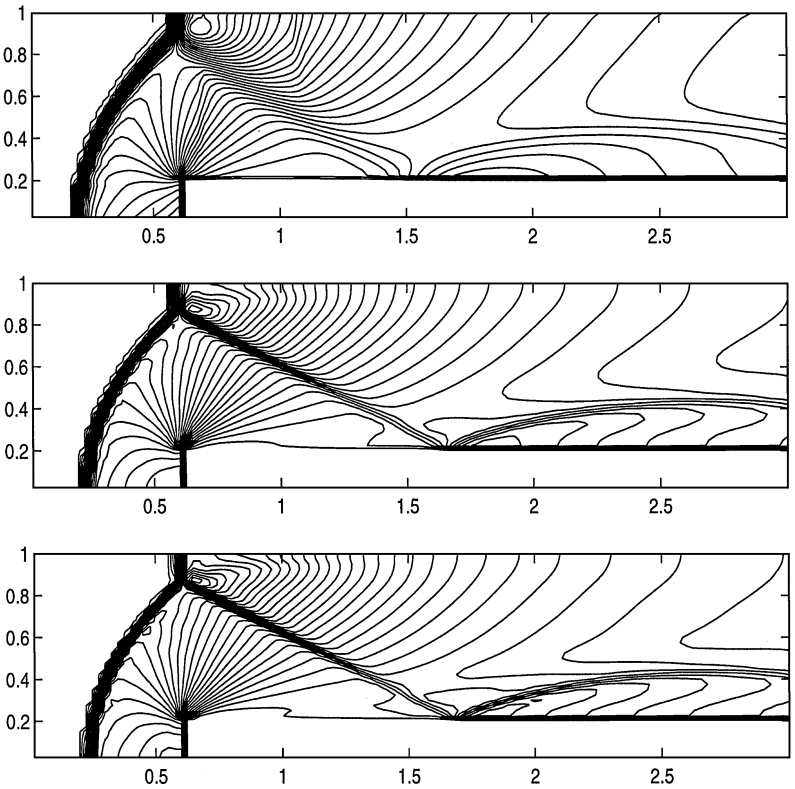

FIG. 10. The relativistic version of Emery's flat-faced step for a time $t = 4.3$. Thirty isocontours of the logarithm of the density for the different reconstructions used: first-order (top), ENO2 (center), and PHM (bottom). The *corner treatment* described in the Appendix has been applied. All cases correspond to an inflow velocity $v_0^x = 0.995$. Computations were performed on a rectangular grid of 120×40 zones.

noticeable in the secondary reflected shock over the step. Figure 11 shows a section plot of the density at $y = 0.4$.

5.2. *A 2D Simulation of a Supersonic Jet*

As a 2D application we have simulated the evolution of a fluid injected supersonically into the computational domain through a small nozzle. This simple initial setup allows for the

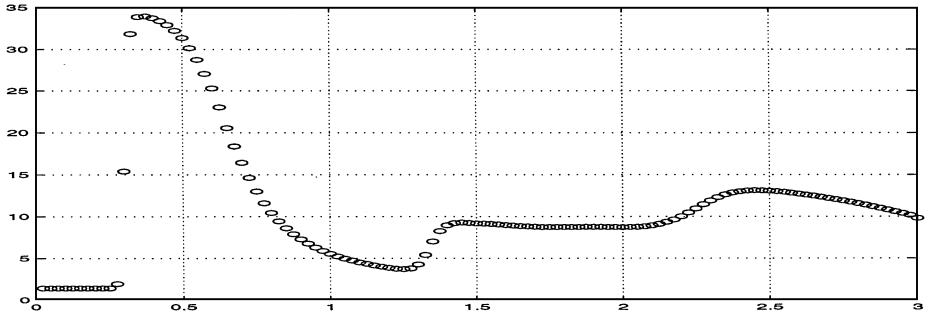

FIG. 11. The relativistic version of Emery's flat-faced step for a time $t = 4.3$. A one-dimensional section ($y = 0.4$) of the density for our ENO2 approximation of Fig. 10.

study of the morphology and dynamics of *relativistic jets* encountered in some astrophysical scenarios. A comprehensive study can be found in [22], where Marquina's solver was used, together with the piecewise-parabolic reconstruction procedure of Woodward and Colella, adapted to the relativistic equations by Martí and Müller in [19].

Here we choose one particular model of the large sample in [22] to illustrate the performance of Marquina's scheme with respect to another linearized solver of Roe's type previously employed in relativistic simulations (see [20]).

We use cylindrical coordinates (r, z) to discretize the numerical domain, which is 25 units long in the z-direction and 7 units wide in the r-direction. The domain is covered by a uniform numerical grid consisting of 500×140 zones. The beam fluid is injected into the grid parallel to the symmetry axis (the z axis) through a nozzle at the bottom ($r = 0$) of the left boundary of the grid ($z = 0$), which is 20 zones wide (i.e., of length unity). Outflow boundary conditions are used at all boundaries, except at the symmetry axis ($r = 0$ boundary), where reflection conditions are imposed, and at the nozzle, where fixed inflow beam conditions are used. The initial model that we consider for the injected beam fluid corresponds to a Mach 6 flow with $\Gamma = 5/3$. The density outside the beam is $\rho = 1$ and the velocity of the fluid at the nozzle is $v^r = 0$ and $v^z = 0.99$.

We apply two different codes to this initial setup. Both codes use the same piecewise-parabolic reconstruction and time-stepping procedures, but one incorporates Marquina's recipe in the numerical flux computation while the other one uses the Roe-type linearized solver used in [20].

Figure 12 shows our numerical approximations obtained at an early stage of the simulation in each case. Even with this simple initial setup the flow develops an interesting structure. In both figures one can see the leading bow shock, the internal contact discontinuity which is Kelvin–Helmholtz unstable, and the beam, the innermost internal channel. At this time of the evolution the beam presents an internal conical shock and a Mach disk at its head, which slows down the material inside the beam.

The most significant difference between both plots is the small protuberance ahead of the bow shock which appears when using the Roe-like solver. This is purely a numerical artifact, since the Mach disk prevents the material inside the beam from pushing other material ahead of the bow shock. This local pathological behavior is well known in blunt body simulations in gas dynamics (see [24] and references therein) and receives the name of *carbuncle*. As pointed out by Quirk [24], Roe's scheme admits sometimes this spurious solution, being the effect more likely to appear for high Mach number flows and the more closely the grid is aligned to the bow shock. This is precisely what we have here. As can be seen in Fig. 12 the pathology seems to disappear when Marquina's solver is used. The price to be paid is a 20% increase in the total computational time when Marquina's flux formula is used in the code.

6. CONCLUSIONS

Marquina's flux formula [4], a new numerical flux formula to compute the flux at a cell interface for hyperbolic systems of conservation laws, is used to describe a new class of HRSC methods and to study its performance and applicability in the field of special relativistic hydrodynamics.

An appropriate conservative formulation for the equations of RFD is the starting point to apply any shock-capturing technique to RFD. In this paper we continue using the

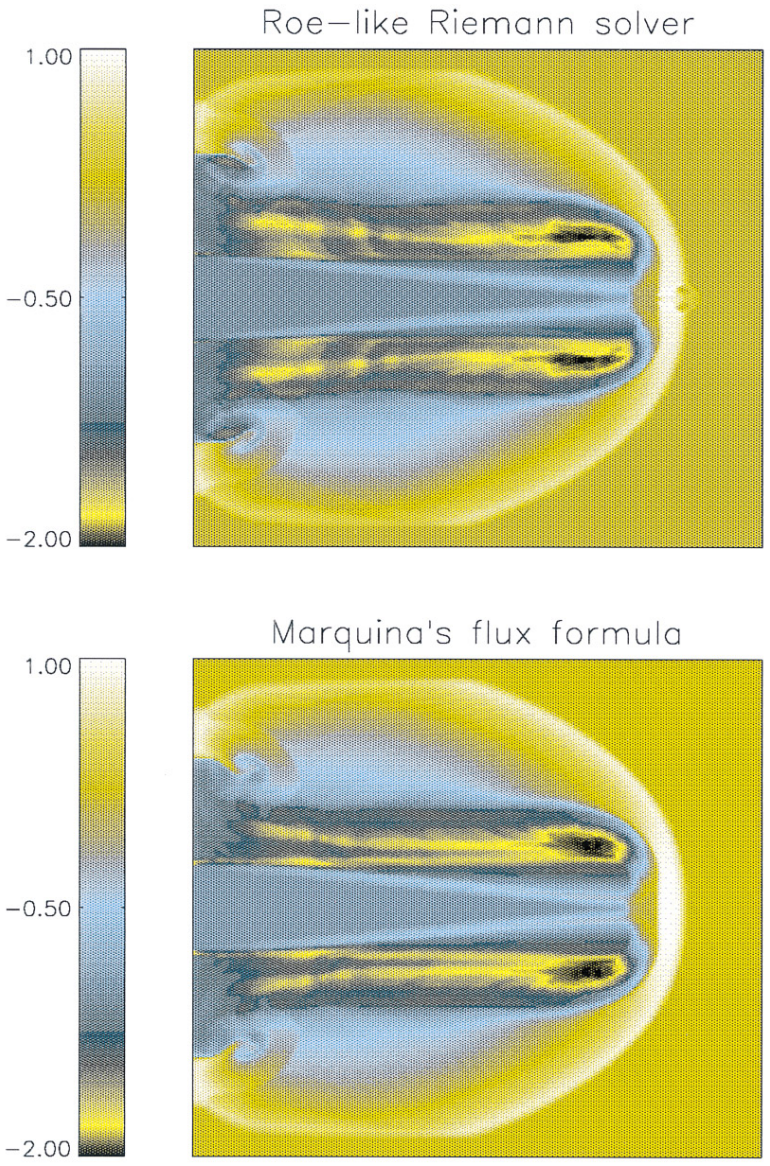

FIG. 12. Simulation of a supersonic relativistic jet; the logarithm of the rest-mass density—gray-scale—obtained with a PPM reconstruction procedure. Top: a linearized Roe-like solver (notice the "carbuncle phenomenon" ahead of the bow shock). Bottom: Marquina's flux formula. The behaviour of the numerical solution agrees with the physics of the problem.

conservative formulation employed in [12, 19, 20, 15, 22], providing for the first time an explicit, ready-to-use, formulation of the full spectral decomposition of the Jacobian matrices associated to the fluxes in each spatial direction. This is an essential ingredient in the HRSC techniques we propose, since the spectral decomposition is used in the flux computation as well as in the reconstruction step. The spectral decomposition has, moreover, the potential interest of allowing an extensive range of application of HRSC methods, with different approaches, i.e, different approximate Riemann solvers.

We have performed several standard one-dimensional shock tube tests and our numerical results confirm the feasibility of our theoretical procedure, as well as our numerical algorithm. The explicit spectral decomposition of the Jacobian matrices given in Section 2 allows us to carry out our higher order reconstructions for locally defined characteristic fields, which seems to be an important ingredient to obtain well behaved profiles in the presence of strong pressure jumps. In all our numerical tests, the behavior of our second- and third-order codes is consistent with what is to be expected of a HRSC method.

Our second- and third-order methods provide accurate, oscillation-free numerical approximations of better quality than those of [26], especially at the corners of rarefaction waves. This is probably due to the fact that special relativistic effects are included in the scheme in a fundamental way, not only by an a priori estimate of two signal velocities. Concerning the comparisons with previous results in [19], we can conclude that our relativistic PHM provides numerical approximations which are similar to their relativistic PPM (also a third-order method). This would imply that, at least for high order methods, nothing is gained by using an exact Riemann solver.

To illustrate the behavior of these schemes in two dimensions, we have studied numerically the flow evolution in a wind tunnel containing a flat-faced step. In our relativistic extension of this classical test in gas dynamics we obtained a well-behaved numerical approximation. In addition we have computed the evolution of a supersonic (and ultrarelativistic) jet stream, obtaining an approximation which appears to be both physically correct and numerically well behaved. This last simulation was done using an *existing* code, substituting the numerical flux computation routine by the one described in this paper. Marquina's flux formula can be easily incorporated into an existing conservative code for the solution of hyperbolic systems of conservation laws (once the spectral decomposition of the Jacobian matrices of the system is known), thus avoiding the daunting task of programming a new method from scratch.

APPENDIX: DISCUSSION OF THE CORNER TREATMENT IN RELATIVISTIC HYDRODYNAMICS

As in the Newtonian case [33, 4], the correction process at the corner of the step is based on the assumption of a nearly steady flow in a small region around the corner.

We shall perform two successive corrections on certain cells (which we call "b") above the step, using the values of the variables at the cell located just to the left and below the corner (we call this call "a"). The "b" cells are the first four cells of the first row above the step, starting just to the right of the corner, and the first two cells of the second row above, also starting from the right.

The corrections in the relativistic case are the natural extension of those in [4] for the Newtonian case. They are as follows:

• *Entropy correction.* In each "b" cell, we reset the density in order for the "pseudo-entropy," $A = P/\rho^{\gamma}$, in cell "b", to be the same as in cell "a":

$$\rho_b = \rho_a \left(\frac{P_b}{P_a} \right)^{1/\gamma}. \tag{24}$$

• *Enthalpy correction.* Using the reset density value, we correct the enthalpy in "b" cells, by changing the magnitudes of the velocities (not their directions!) as follows:

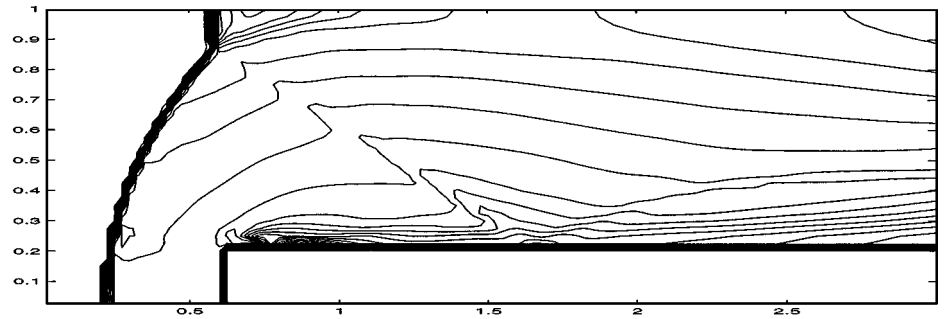

FIG. 13. The relativistic version of Emery's flat-faced step for a time $t = 4.3$ and an inflow velocity $v_0^x = 0.995$. Thirty isocontours of the pseudo-entropy for our third-order PHM reconstruction. The corner correction has been implemented.

There is always a nonnegative constant α such that

$$H_a = H_b^{\alpha}, \tag{25}$$

where H_a stands for the value of hW in cell "a," and

$$H_b^{\alpha} \equiv h_b W_b^{\alpha} = \frac{1}{\sqrt{1-\alpha q_b^2}}\left(1 + B\rho_b^{\gamma-1}\right) \tag{26}$$

with q_b^2 being the sum of the squares of the original components of the velocity in cell "b" and B being $A\gamma/(\gamma-1)$. Equation (25) is just *Bernouilli's law* for relativistic flows [13], and it always has a nonnegative solution for α, because the value of the density in "b" cells is never larger than the value in cell "a":

$$\alpha = \frac{1}{q_b^2}\left[1 - \left(1 - q_a^2\right)\left(\frac{1 + B\rho_b^{\gamma-1}}{1 + B\rho_a^{\gamma-1}}\right)^2\right]. \tag{27}$$

Obviously, the Newtonian limit [4] is covered.

We then reset the vector **u** in each "b" cell to

$$\left(\rho_b W_b^{\alpha},\, \rho_b h_b \left(W_b^{\alpha}\right)^2 \sqrt{\alpha}(q_b)^j,\, \rho_b h_b \left(W_b^{\alpha}\right)^2 - p_b - \rho_b W_b^{\alpha}\right). \tag{28}$$

If these two successive corrections are not applied, the entropy is violated along the streamlines just above the step.

In Figs. 13 and 14 we display two contour plots of the pseudo-entropy, A, at $t = 4.3$. They correspond to numerical approximations obtained with the our PHM-third-order code. Figure 13 corresponds to the application of the corner treatment and Fig. 14 to the absence of corner treatment. We have observed that, when no treatment is applied, the value of the enthalpy above and near the corner is slightly smaller than the value at the left of the corner. The fluid around the corner is almost steady; however, the entropy is clearly violated. The section $y = 0.2$ of the pseudo-entropy is shown in Figs. 15 and 16 for both cases. We observe a strong entropy violation at $x = 0.6$, the abscissa of the corner, which can be considered nearly a streamline of the flow. When the corner treatment is applied, there are no sudden entropy jumps except for the expected entropy production at the bow shock.

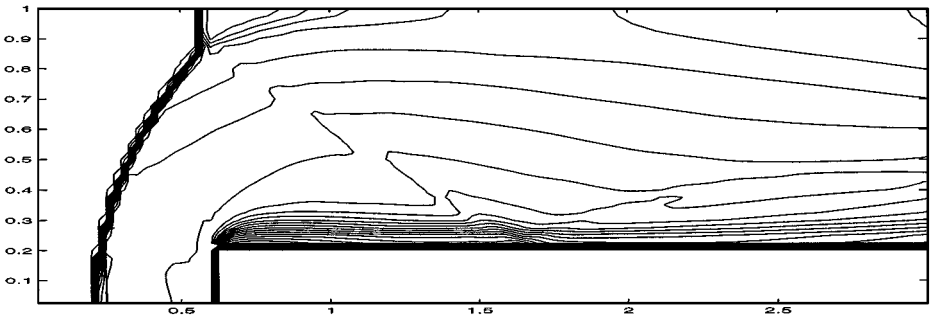

FIG. 14. The relativistic version of Emery's flat-faced step for a time $t = 4.3$ and an inflow velocity $v_0^x = 0.995$. Thirty isocontours of the pseudo-entropy for our third-order PHM reconstruction. The corner correction has not been implemented and we observe the buildup of a numerical boundary layer.

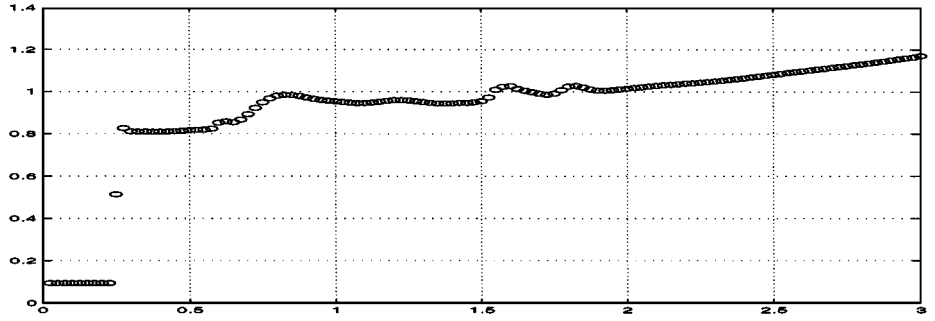

FIG. 15. The relativistic version of Emery's flat-faced step for a time $t = 4.3$. A one-dimensional section ($y = 0.2$) of the pseudo-entropy for our third-order PHM reconstruction of Fig. 13.

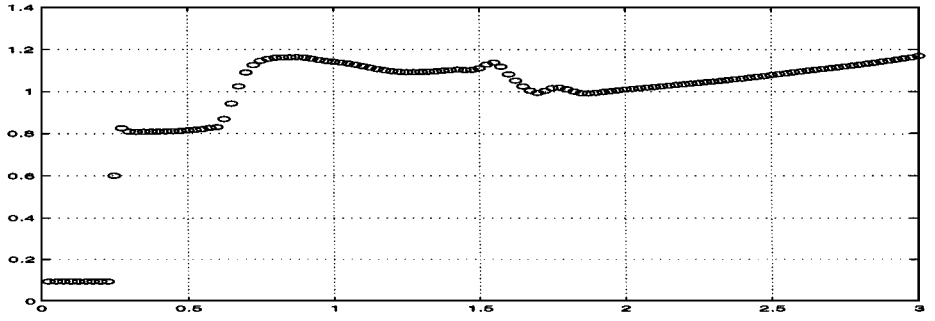

FIG. 16. The relativistic version of Emery's flat-faced step for a time $t = 4.3$. A one-dimensional section ($y = 0.2$) of the pseudo-entropy for our third-order PHM reconstruction of Fig. 14.

ACKNOWLEDGMENTS

The authors thank J. Mª Martí for many useful discussions as well as a large amount of good advice. His permission to use his codes in our astrophysical simulation is gratefully acknowledged. This work has been supported by the Spanish DGICYT (Grants PB94-0973 and PB94-0987); the fourth author has also been partially supported by an ARPA URI Grant ONR-N00014-92-J-1890. Calculations were carried out in HP workstations (Apollo 9000, series 700). The authors acknowledge a grant from the Instituciò Valenciana d'Estudis i Investigaciò.

REFERENCES

1. A. M. Anile, *Relativistic Fluids and Magneto-Fluids* (Cambridge Univ. Press, Cambridge, 1989).
2. D. Balsara, *J. Comput. Phys*. **114**, 284 (1994).
3. F. Banyuls, J. A. Font, J. M. Ibañez, J. M. Martí, and J. A. Miralles, *Astrophys. J.* **476**, 221 (1997).
4. R. Donat and A. Marquina, *J. Comput. Phys*. **125**, 42 (1996).
5. G. C. Duncan and P. A. Hughes, *Astrophys. J.* **436**, L119 (1994).
6. A. Dolezal and S. S. M. Wong, *J. Comput. Phys.* **120**, 266 (1995).
7. A. F. Emery, *J. Comput. Phys.* **2**, 306 (1968).
8. F. Eulderink, Ph.D. thesis, University of Leiden, 1993.
9. F. Eulderink and G. Mellema, *Astron. Astrophys.* **284**, 652 (1994).
10. R. Fedkiw, B. Merryman, R. Donat, and S. Osher, UCLA CAM Report **96-18**, 1996.
11. J. A. Font, Ph.D. thesis, University of Valencia, 1994.
12. J. A. Font, J. Mª. Ibáñez, A. Marquina, and J. Mª. Martí, *Astron. Astrophys.* **282**, 304 (1994).
13. L. D. Landau and E. M. Lifshitz, *Fluid Mechanics* (Pergamon, Elmsford, NY, 1975).
14. R. J. LeVeque, *Numerical Methods for Conservation Laws* (Birkhäuser, Basel, 1991).
15. A. Marquina, J. Mª. Martí, J. Mª. Ibáñez, J. A. Miralles, and R. Donat, *Astron. Astrophys.* **258**, 566 (1992).
16. A. Marquina, *SIAM J. Sci. Comput.* **15**, 892 (1994).
17. J. Mª. Martí, J. Mª. Ibáñez, and J. A. Miralles, *Phys. Rev. D* **43**, 3794 (1991).
18. J. Mª. Martí and E. Müller, *J. Fluid Mech.* **258**, 317 (1994).
19. J. Mª. Martí and E. Müller, *J. Comput. Phys*. **123**, 1 (1996).
20. J. Mª. Martí, E. Müller, and J. Mª. Ibáñez, *Astron. Astrophys.* **281**, L9 (1994).
21. J. Mª. Martí, E. Müller, J. A. Font and J. Mª. Ibáñez, *Astrophys. J.* **448**, L105 (1995).
22. J. Mª. Martí, E. Müller, J. A. Font, J. Mª. Ibáñez, and A. Marquina, *Astrophys. J.* **479**, 151 (1997).
23. M. L. Norman and K.-H. A. Winkler, in *Astrophysical Radiation Hydrodynamics*, edited by M. L. Norman and K.-H. A. Winkler (Reidel, Dordrecht, 1986).
24. J. Quirk, *Int. J. Numer. Methods Fluids* **18**, 555 (1994).
25. R. D. Richtmyer and K. W. Morton, *Difference Methods for Initial-Value Problems* (Interscience, New York, 1967).
26. V. Schneider, V. Katscher, D. H. Rischke, B. Waldhauser, J. A. Marhun, and C.-D. Munz, *J. Comput. Phys.* **105**, 92 (1993).
27. C. W. Shu and S. J. Osher, *J. Comput. Phys.* **83**, 32 (1989).
28. R. E. Spencer and S. J. Newell, *Vistas Astronom.* **41**, 1 (1997).
29. R. B. Clare and D. Strottman, *Phys. Rep.* **141**, 177 (1986).
30. D. Strottman, in *The Nuclear Equation of State, Part B*, edited by W. Greiner and H. Stöcker (Plenum, New York, 1989).
31. L. Wen, A. Panaitescu, and P. Laguna, Preprint astro-ph/9612045v2 (1997).
32. J. R. Wilson, *Astrophys. J.* **173**, 431 (1972).
33. P. R. Woodward and P. Colella, *J. Comput. Phys.* **54**, 115 (1984).